Localized Surface Plasmon Resonance Nanosensor: A High-Resolution Distance-Dependence Study Using Atomic Layer Deposition

Alyson V. Whitney,[†] Jeffrey W. Elam,[‡] Shengli Zou,[†] Alex V. Zinovev,[§] Peter C. Stair,[†] George C. Schatz,[†] and Richard P. Van Duyne*,[†]

Department of Chemistry, Northwestern University, 2145 Sheridan Road, Evanston, Illinois 60208-3113, and Energy Systems Division and Materials Science Division, Argonne National Laboratory, 9700 S. Cass Ave., Argonne, Illinois 60439

Received: July 22, 2005; In Final Form: August 30, 2005

Atomic layer deposition (ALD) is used to deposit 1−600 monolayers of Al_2O_3 on Ag nanotriangles fabricated by nanosphere lithography (NSL). Each monolayer of Al_2O_3 has a thickness of 1.1 Å. It is demonstrated that the localized surface plasmon resonance (LSPR) nanosensor can detect Al_2O_3 film growth with atomic spatial resolution normal to the nanoparticle surface. This is approximately 10 times greater spatial resolution than that in our previous long-range distance-dependence study using multilayer self-assembled monolayer shells. The use of ALD enables the study of both the long- and short-range distance dependence of the LSPR nanosensor in a single unified experiment. Ag nanoparticles with fixed in-plane widths and decreasing heights yield larger sensing distances. X-ray photoelectron spectroscopy, variable angle spectroscopic ellipsometry, and quartz crystal microbalance measurements are used to study the growth mechanism. It is proposed that the growth of Al_2O_3 is initiated by the decomposition of trimethylaluminum on Ag. Semiquantitative theoretical calculations were compared with the experimental results and yield excellent agreement.

Introduction

The localized surface plasmon resonance (LSPR) wavelength shift response, $\Delta\lambda_{max}$, of Ag nanoparticles fabricated by nanosphere lithography (NSL) has been used to develop a new class of nanoscale optical biosensors.[1−5] On the most elementary level, the LSPR wavelength shift response of these sensors can be understood using a model of the refractive-index response of propagating surface plasmons on a planar noble metal surface[6]

$$\Delta\lambda_{max} = m\Delta n[1 - \exp(-2d/l_d)] \quad (1)$$

where $\Delta\lambda_{max}$ is the wavelength shift, m is the refractive-index sensitivity, Δn is the change in refractive index induced by an adsorbate, d is the effective adsorbate layer thickness, and l_d is the characteristic electromagnetic field decay length. This model assumes a single exponential decay of the electromagnetic field normal to the planar surface, which is accurate for a propagating surface plasmon but is undoubtedly an oversimplification for the electromagnetic fields associated with noble metal nanoparticles. While this oversimplified model does not quantitatively capture all aspects of the LSPR nanosensor response, it does provide some guidance for sensor optimization. In particular, eq 1 highlights the importance of distance dependence as described by the electromagnetic field decay length, l_d.

Haes and co-workers explored the long-range distance dependence of the LSPR nanosensor using self-assembled monolayers (SAMs) of 11-mecaptoundecanoic acid (11-MUD) and Cu^{2+} ions adsorbed on arrays of noble metal nanoparticles with various sizes, shapes, and compositions.[7] The spatial resolution of this experiment was limited to the thickness of the 11-MUD/Cu^{2+} monolayer which was at least 1.6 nm. Several interesting characteristics of the long-range behavior were found including (1) the LSPR shift vs SAM thickness is nonlinear; (2) Ag nanoparticles are more sensitive than Au nanoparticles; (3) nanotriangles have larger sensing distances than nanohemispheroids; (4) increasing the nanoparticle in-plane width results in larger sensing distances; (5) decreasing nanoparticle out-of-plane height results in larger sensing distances.[7] Semiquantitative theoretical calculations revealed that the plasmon resonance shift is controlled by the average electromagnetic field over the nanoparticle surface.[7]

Similarly, the short-range distance dependence (0−3 nm) of the LSPR nanosensor has been studied using alkanethiol, CH_3-$(CH_2)_x$SH (x = 2−11, 13−15, and 17), monolayers.[8,9] It was found that eq 1 does a remarkably good job of accounting for the short-range LSPR response if one assumes a value l_d = 5−6 nm. In addition, the dependence of $\Delta\lambda_{max}$ on the chain length of the alkanethiol monolayer was found to be linear, with a large slope of 3.1−3.3 nm per CH_2 unit.[9]

Even though much important information was obtained from these previous long- and short-range distance dependence studies, it was hypothesized that new information could be obtained if it were possible to deposit single layers of a material with thicknesses of ∼1 Å. Furthermore, while the refractive index of the bulk SAM molecule is known, the refractive index of the SAM is not known making an accurate theoretical model of the experiment difficult.[7]

Atomic layer deposition (ALD) is just such a fabrication method that produces highly uniform and controlled thin films. Precursor gases are alternately pulsed through the reactor and purged away resulting in a self-limiting growth process that constructs a film one monolayer at a time.[10] Highly uniform monolayers of Al_2O_3 can be deposited with ∼1 Å thickness

* To whom correspondence should be addressed. E-mail: vanduyne@chem.northwestern.edu.
[†] Department of Chemistry, Northwestern University.
[‡] Energy Systems Division, Argonne National Laboratory.
[§] Materials Science Division, Argonne National Laboratory.

10.1021/jp0540656 CCC: $30.25 © xxxx American Chemical Society
Published on Web 00/00/0000 PAGE EST: 6.1

resolution and a refractive index of 1.57.[11,12] Depositing Al_2O_3 multilayers onto the noble metal nanosensor should allow the long-range distance dependence of the LSPR nanosensor to be probed with 10x spatial resolution compared with previous work.[7]

In this paper, we have utilized ALD of Al_2O_3 to probe both the long- and short-range LSPR distance dependences of Ag nanoparticles in one integrated experiment. The following results are presented: (1) A detailed study of the long-range distance dependence of the LSPR sensor with 10x increased spatial resolution afforded by ALD in comparison with earlier experiments with SAMs; (2) LSPR nanosensors are shown to have single Al_2O_3 layer detection capabilities; (3) at short range, triangular nanoparticles with fixed widths and smaller out-of-plane heights have larger LSPR sensing distances. A semiquantitative theoretical analysis of the long- and short-range distance dependence of the LSPR sensor is presented. Furthermore, the nucleation and growth of Al_2O_3 on Ag surfaces was studied using quartz crystal microbalance (QCM), variable angle spectroscopic ellipsometry (VASE), and X-ray photoelectron spectroscopy (XPS) measurements. These measurements reveal that the Al_2O_3 deposits on the LSPR Ag surface in a layer-by-layer fashion and the initial nucleation may proceed via the thermal decomposition of trimethylaluminum (TMA) on Ag.

Experimental Methods

Materials. Ag (99.99%) was purchased from D. F. Goldsmith (Evanston, IL). Borosilicate glass substrates, no. 2 Fisherbrand 18-mm circular coverslips, were acquired from Fisher Scientific (Pittsburgh, PA) and P-doped Si(111) was obtained from Wacker Siltronic (Portland, OR). Hexanes, methanol, H_2SO_4, H_2O_2, and NH_4OH were purchased from Fischer Scientific (Fairlawn, VA). Surfactant-free carboxyl-terminated polystyrene nanospheres with 390 nm (±19.5 nm) diameters were received in a suspension of water from Duke Scientific (Palo Alto, CA). Absolute ethanol was acquired from Pharmco (Brookfield, CT). Millipore cartridges (Marlbourough, MA) were used to purify water to a resistivity of 18 MΩ cm^{-1}. Al_2O_3 films were fabricated by ALD utilizing TMA purchased from Sigma Aldrich (Milwaukee, WI) and deionized water.

Nanosphere Lithography. NSL was used to fabricate monodispersed, surface-confined Ag nanoparticles.[13] Glass and Si(111) substrates were cleaned in a piranha etch solution (30% 3:1 H_2SO_4/H_2O_2) for 30 min at 80 °C. After rinsing with water, the substrates were sonicated for 60 min in 5:1:1 $H_2O/H_2O_2/NH_4OH$ in order to create a hydrophilic surface on the substrate to facilitate self-assembly of the nanosphere masks. Finally, the substrates were rinsed and stored in water for future use. Two-dimensional SAM masks of nanospheres were fabricated by drop-coating approximately 2.5 μL of undiluted nanosphere solution (10% solid) on the pretreated substrates. The nanospheres were allowed to dry in ambient conditions. Ag was deposited by electron beam (e-beam) deposition in a Kurt J. Lesker Axxis e-beam deposition system (Pittsburgh, PA) with a base pressure of 10^{-6} Torr. The mass thickness and deposition rate (1 Å/s) were monitored using a Sigma Instruments 6 MHz gold plated QCM (Fort Collins, CO). After the Ag deposition, the nanosphere masks were removed by sonication in absolute ethanol for 3 min. Hemispheroidal Ag nanoparticles were fabricated by annealing Ag triangular nanoparticles at 300 °C for 1 h at ~1 Torr under N_2.

Nanoparticle Annealing. The Ag nanoparticles were solvent annealed using hexanes and methanol in a home-built flow cell to ensure the stabilization of the LSPR extinction spectra.[8] Dry

SCHEME 1

$$\text{(A) Al-OH}^* + \text{Al(CH}_3)_3 \rightarrow \text{Al-O-Al(CH}_3)_2^* + \text{CH}_4$$

$$\text{(B) Al-CH}_3^* + \text{H}_2\text{O} \rightarrow \text{Al-OH}^* + \text{CH}_4$$

*Signifies the surface species.

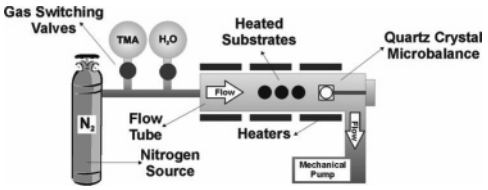

Figure 1. Schematic representation of ALD System.

N_2 gas and solvent were cycled through the flow cell until the λ_{max} of the nanoparticle arrays were stabilized. The samples were then rinsed with absolute ethanol and dried under N_2.

Atomic Layer Deposition. Al_2O_3 films were fabricated on the Ag nanoparticles by ALD. The reactor utilized in these experiments is similar to previous publications.[14] TMA and deionized H_2O vapors were alternately pulsed through the reaction chamber utilizing N_2 as the carrier gas at a mass flow rate of 360 sccm and a pressure of 1 Torr using a growth temperature of 50 °C. Al_2O_3 ALD proceeds on a hydroxylated surface according to Scheme 1.[12]

Figure 1 depicts a simplified schematic diagram of the ALD reactor. One complete AB cycle is 42 s: (1) TMA reactant exposure time = 1 s, (2) N_2 purge following TMA exposure time = 10 s, (3) H_2O reactant exposure time = 1 s, and (4) N_2 purge following H_2O exposure time = 30 s. Long purge times are necessary at low temperatures to prevent chemical vapor deposition (CVD) of Al_2O_3.[12]

X-Ray Photoelectron Spectroscopy. The surface composition of a 50 nm Ag film deposited by e-beam on glass was analyzed by XPS. The measurements were performed using Mg Kα (1253.6 eV) radiation and a hemispherical electron energy analyzer (HEA). The spectra were recorded in fixed absolute resolution mode of the HEA with pass energy of 44 eV (for survey spectra) and 22 eV (for detailed measurements of core level peaks). The electrons were collected from the area with an elliptical shape with dimensions of 4 mm × 3 mm. Survey spectra with an energy step of 1 eV and precision measurements of core level photoelectron lines O1s and Ag3d as well as a valence band with the energy step of 0.2 eV were recorded. The spectrometer calibration was performed using the gold XPS emission line ($Au4f_{7/2}$ with a binding energy of 84 eV). The residual vacuum in the analyzing chamber was 4×10^{-10} mbar. Processing of the obtained XPS spectra was performed using the CasaXPS software. All measured peaks were corrected for inelastic scattering by subtracting the Shirley background from the raw spectra, followed by the fitting of peaks by using the asymmetric pseudo-Voigt shaped peaks with a different relative content of Gaussian and Lorentzian components.

Variable Angle Spectroscopic Ellipsometry. Al_2O_3 film thicknesses were measured by VASE using an M-2000V from J. A. Wollam Co. VASE measurements were taken on Al_2O_3 ALD films fabricated on a 50 nm Ag film deposited by an e-beam. The Al_2O_3 ALD on the Ag film was done concurrently with Al_2O_3 ALD on the Ag nanoparticles.

Quartz Crystal Microbalance Measurements. Details of the in situ QCM measurements have been reported previously.[14] Briefly, the QCM experiments utilized polished sensors (Colorado Crystal Corporation, Part #CCAT1BK-1007-000) installed

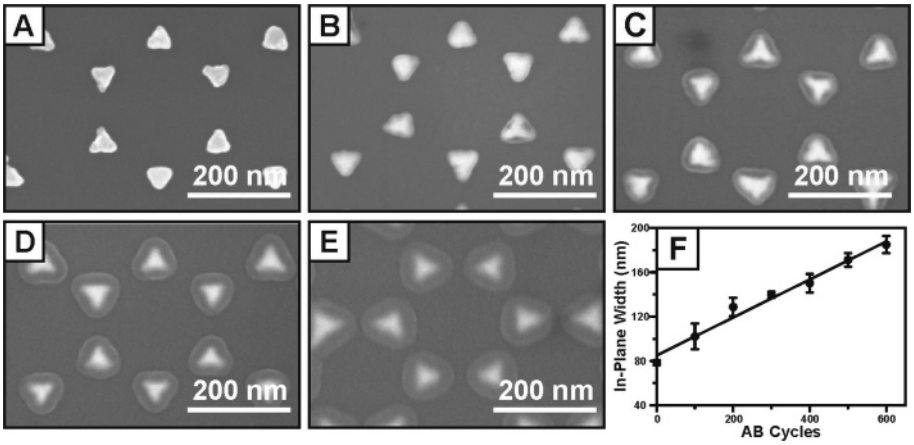

Figure 2. SEM images of (A) bare Ag nanoparticles ($a = 90$ nm, $b = 51$ nm) and Ag nanoparticles following (B) 100, (C) 200, (D) 400, and (E) 600 AB cycles of TMA/ H_2O. (F) Plot of in-plane width of Ag nanoparticle AB cycles determined from the SEM images.

in a Maxtek BSH-150 bakeable sensor head. Prior to installation, an Ag film with a thickness of 50 nm was deposited onto the QCM sensor by e-beam. To prevent deposition on the back surface of the sensor during the ALD experiments, the sensor housing was continuously purged with ultrahigh purity N_2 and the gap between the front surface of the sensor and the crystal holder was filled using a high-temperature conducting epoxy (Epotek P1011). To minimize temperature-induced apparent mass changes, a uniform temperature distribution was established near the QCM by adjusting the temperature setpoints and heater power distribution of four separate temperature-controlled heating zones.[15] The QCM signals were monitored using a Maxtek TM400 thickness monitor with a mass resolution of 0.375 ng/cm^2 (0.01 Å Al_2O_3) at 10 measurements per second.

UV−Vis Extinction Spectroscopy. LSPR extinction measurements of the Ag nanoparticle arrays were obtained using the M-2000V in transmission mode.

Scanning Electron Microscopy (SEM). Various Al_2O_3 film thicknesses on triangular Ag nanoparticles on Si(111) were observed with a Hitatchi S-4700-II SEM. Images were collected with 10.0 kV.

Results and Discussion

SEM of Ag Nanotriangles. SEM images of bare and Al_2O_3-coated Ag nanotriangles on Si(111) were acquired. Si(111) was chosen as the substrate to minimize charging and to produce high-quality images. Nanoparticles fabricated on Si(111) substrates are similar to those fabricated on glass substrates. Figure 2 presents SEM images of bare Ag nanoparticles (Figure 2A) and Ag nanoparticles coated by Al_2O_3 ALD using 100 (Figure 2B), 200 (Figure 2C), 400 (Figure 2D), and 600 (Figure 2E) AB cycles. Figure 2F depicts a plot of the nanoparticle in-plane width vs AB cycles determined from the SEM images and yields a growth rate of 0.9 Å/cycle.

Ellipsometry. VASE studies were carried out to accurately monitor the Al_2O_3 film thickness and growth rate. Measurements were carried out on a 50 nm Ag film e-beam deposited on glass. Figure 3 plots the Al_2O_3 film thickness vs AB cycles of TMA and water deposited on a Ag-coated Si(111) surface measured with VASE. VASE data is presented for 0−425 AB cycles (Figure 3A). Two growth rates are observed: the growth rate for 0−20 AB cycles = 1.65 Å per cycle (Figure 3A-1) and the growth rate for 20−425 AB cycles = 0.98 Å per cycle (Figure 3A-2). Figure 3B depicts the VASE data for just the 0−20 AB cycles. Both growth rates are extremely linear with $R^2 = 0.9934$ and 0.9998 for (Figure 3A-1) and (Figure 3A-2), respectively,

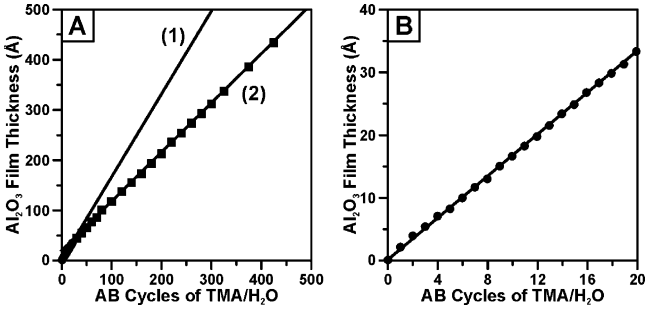

Figure 3. Ellipsometry measurements for Al_2O_3 ALD grown on a 50 nm Ag film. (A) Ellipsometry data for 0−425 AB cycles of TMA and water. Circles denote single AB cycles of TMA, and water and squares denote multiple AB cycles of TMA and water. (B) Ellipsometry data for 0−20 AB cycles of TMA and water. Circles denote single AB cycles of TMA and water. The growth rate for 0−20 AB cycles (1) = 1.65 Å per cycle. The growth rate for 30−425 AB cycles (2) = 0.98 Å per cycle.

and can therefore be easily predicted and controlled. The higher growth rate (1.65 Å per cycle) measured during the first 20 AB cycles is a consequence of a much larger H_2O exposure resulting from removing the sample from the reaction chamber and exposing the sample to room air after each AB cycle to collect an extinction spectrum. The Al_2O_3 ALD growth rate increases with increasing water exposures.[16] The growth rate then reduces to 0.98 Å per cycle once multiple AB cycles of TMA and water are employed (Figure 3A-2). This growth rate is very close to the value determined from the SEM measurements (Figure 2F) and is typical for ALD Al_2O_3 on hydroxylated SiO_x under these conditions.[12] Modeling of the VASE data yields a refractive index for the ALD Al_2O_3 of $n = 1.57$.

XPS Measurements on Ag Film. Given that the Al_2O_3 ALD growth mechanism requires surface hydroxyl groups (Scheme 1), it was surprising that the Al_2O_3 ALD proceeds at the same rate on Ag as on hydroxylated SiO_x without apparent inhibition or nucleation delay. Hydroxyl groups may be present if the Ag surface is oxidized; however, VASE detected no AgO before or after the Al_2O_3 ALD. Further measurements were made using XPS, an extremely sensitive probe for surface composition. XPS was performed on a 50 nm Ag film e-beam deposited on glass. Figure 4 presents XPS measurements on a 50 nm Ag film e-beam deposited on glass obtained before (Figure 4A) and after (Figure 4B) annealing the Ag film at ∼200 °C for 40 min under ultrahigh vacuum. Figure 4A shows 10.5% oxygen content on the surface of the Ag film. After the substrate is annealed, the oxygen content on the Ag film surface drops to 5.6% (Figure

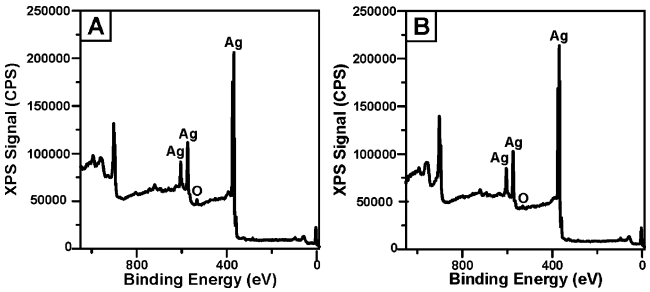

Figure 4. XPS measurements on 50 nm Ag film. (A) XPS measurements taken on the Ag film as deposited. 10.5% oxygen was found on the Ag film surface. (B) XPS measurements taken on the Ag film after annealing for 40 min under UHV at ~200 °C. 5.6% oxygen was on the Ag film surface.

4B). The oxygen XPS peak does not appear at the expected position for AgO (~528−532 eV) indicating that the oxygen peak results from surface impurities.[17]

QCM Measurements on Ag Film. Further exploration of the Al_2O_3 growth mechanism on Ag was done by QCM studies (Figure 5). QCM measurements were conducted on a 50 nm Ag film e-beam deposited directly on the QCM crystal. Figure 5A shows the QCM measurements recorded during 100 AB cycles of Al_2O_3 ALD. The QCM signals have been converted to Al_2O_3 thickness assuming a density of 2.6 g/cm^3.[18] The Al_2O_3 growth is extremely linear with a growth rate of 1.0 Å/cycle in excellent agreement with the VASE and SEM results. Moreover, there is no indication of inhibited initial growth as might be expected for Al_2O_3 ALD on a noble metal surface. The steplike structure in Figure 5A reflects the discrete mass changes produced by the individual TMA and H_2O exposures. Expanded views of the QCM data at early and late times are given in parts B and C of Figure 5 , respectively. The shaded areas represent the time periods that the TMA and water dosing valves were open.

The QCM structure in Figure 5B reveals details about the mechanism for Al_2O_3 nucleation and growth on Ag. Figure 5B shows a large thickness change of 3−4 Å during the first TMA exposure. Given that XPS and VASE detect no AgO and little surface oxygen, the TMA must react directly with the Ag. Although this reaction has not been studied, TMA reacts with Ni(111) to form a monolayer of $Al(CH_3)_2$ and CH_3 surface species even at a low temperature of 110 K.[19] During the initial Al_2O_3 ALD cycles on Ag, the thickness decreases during the TMA purge periods (Figure 5B). This may be a result from the reaction of surface methyl groups and the subsequent desorption of methane. In situ quadrupole mass spectrometry measurements would verify these desorption processes.[20]

There is a net thickness decrease following the H_2O doses and purges at early times (Figure 5B) and a net thickness increase at later times (Figure 5C). This net change reflects the density of surface OH groups: larger net increases result from larger OH group coverages.[20] The net thickness change is negative in Figure 5B because there are no OH groups on the metallic Ag surface. However, the net thickness change is positive (Figure 5C) because the ALD Al_2O_3 surface is fully hydroxylated at 50 °C. Approximately 20 AB cycles are required for the net thickness to reach the steady-state value shown in Figure 5C.

To summarize, our results indicate nearly ideal layer-by-layer growth of the ALD Al_2O_3 on the Ag surfaces. Both the VASE and QCM measurements (Figures 3 and 5) demonstrate highly linear Al_2O_3 growth on planar Ag surfaces without any initial delay. The nucleation may result in part from the reaction of TMA with surface hydroxyls bound to a thin native oxide layer on the Ag. However, the coverage of this oxide layer must be very small (<10%) as shown by XPS (Figure 4). Alternatively, nucleation may occur by the direct reaction of TMA with the Ag surface, and evidence for this mechanism is given by the large, initial mass increase shown in the QCM data (Figure 5b). The SEM analysis also supports layer-by-layer Al_2O_3 growth on the Ag nanoparticles (Figure 2). These results greatly simplify the interpretation of the LSPR spectroscopy of the Ag nanoparticles because the thickness of the Al_2O_3 overlayers can be deduced easily from the number of ALD cycles.

LSPR Spectroscopy of Ag Nanoparticles. Figure 6 depicts LSPR extinction spectra for triangular Ag nanoparticles with an in-plane width (a) of 90 nm and out-of-plane height (b) of 40 nm. The UV−vis spectra for Ag nanoparticles with 0−450 cycles of TMA and water are presented in Figure 6. As subsequent ALD Al_2O_3 layers are completed, the LSPR λ_{max} position red shifts which is consistent with previous work.[7] Importantly, these results clearly demonstrate that the LSPR nanosensor has sufficient sensitivity to detect the deposition of each successive Al_2O_3 monolayer. For nanoparticles with $a = 90$ and $b = 40$ nm, a 5 nm LSPR λ_{max} shift is observed with 2 Å of Al_2O_3. Furthermore, by extrapolation it should be possible to detect submonolayers of material. ALD of Al_2O_3 allows for the fabrication of angstrom thick monolayers which gives this work a 10x increase in the spatial resolution compared to previous work.[7]

LSPR Shifts vs Al_2O_3 Film Thickness. Figure 7 depicts plots of the LSPR λ_{max} shift vs Al_2O_3 film thickness for triangular nanoparticles with $a = 90$ nm and $b = 30$ nm (1), 40 nm (2), 51 nm (4), and hemispheroidal nanoparticles with $a = 104$ nm and $b = 54$ nm (3). In Figure 7A, the LSPR λ_{max} shift vs Al_2O_3 film thickness response is shown for 0−600 AB cycles. These results compare well with previous work.[7] At short distances from the nanoparticle surface, the LSPR λ_{max} shift follows a steep linear slope, but as the distance from the nanoparticle increases, the curve bends over and eventually levels off once the nanoparticle has reached its saturation point. As the nanoparticle height decreases and the in-plane width remains constant, the LSPR λ_{max} shift increases which again agrees with previous results.[7] The short-range distance dependence is highlighted in Figure 7B which depicts the λ_{max} shift vs Al_2O_3 film thickness response for the first 0−20 AB cycles. After each cycle, a LSPR extinction spectrum was collected which presents a highly detailed view of the short-range distance dependence of the LSPR nanosensor. Because Al_2O_3 layers deposited by ALD are ~1.1 Å in thickness,[11] this is the first time that extremely detailed pictures of both the short- and long-range distance dependences of the LSPR nanosensor have been obtained in a single integrated experiment. In fact, the results in this work show that at short distances from the nanoparticle surface, the LSPR λ_{max} shift vs layer thickness follows a steep linear trend compared with the moderate slope at a larger distance from the nanoparticle surface. Nanoparticles with fixed in-plane widths and decreasing out-of-plane heights yield larger sensing distances (Figure 7B-1) as have been observed at larger distances from the nanoparticle surface.[7] The scatter in these plots results from slight misalignments resulting from repositioning the LSPR samples between measurements as the samples were moved between the ALD reactor and the spectrometer. We expect the scatter to be reduced greatly if the extinction spectra are recorded in situ, and work is currently underway to construct a new ALD reactor with in situ optical capability. Nevertheless, the data in Figures 6 and 7 clearly demonstrate

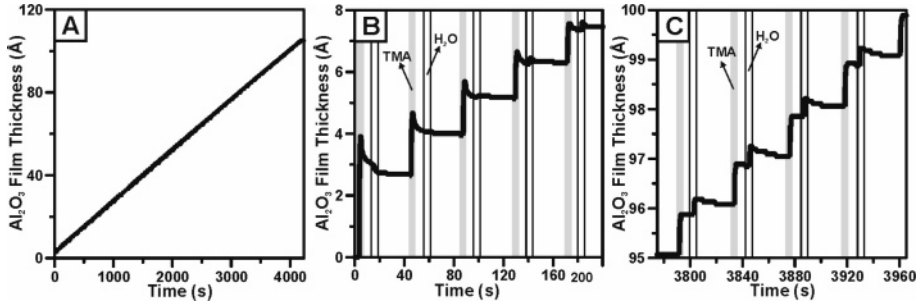

Figure 5. Plots of Al_2O_3 growth rate and QCM step ratio vs AB cycles of TMA and water measured with QCM on 50 nm Ag film. (A) QCM measurements for 0−100 AB cycles of TMA and water. (B) QCM measurements for the first 5 AB cycles of TMA and water. (C) QCM measurements for the final AB cycles of TMA and water. 50 nm Ag was deposited on the QCM to ensure a similar experimental environment. The shaded areas represent the time periods that the TMA and water dosing valves were open.

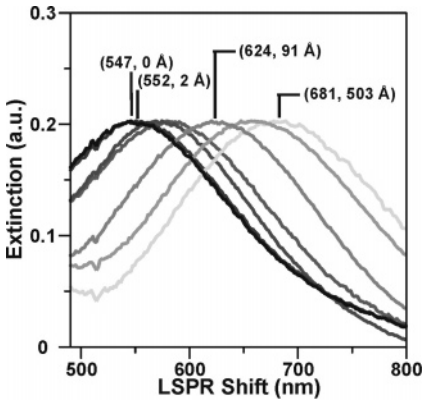

Figure 6. LSPR spectroscopy of Ag nanoparticles ($a = 90$ nm, $b = 40$ nm) for 0−450 AB cycles of TMA and water.

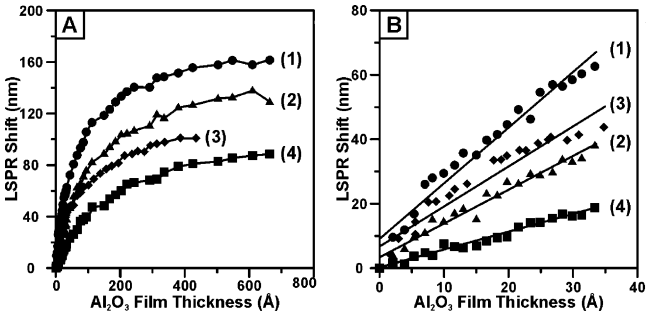

Figure 7. LSPR shift vs Al_2O_3 film thickness. (A) Out-of-plane height dependence on the long- and short-range distance dependence for Ag triangular nanoparticles $a = 90$ nm and $b =$ (1) 30, (2) 40, and (4) 51 nm and Ag hemispherical nanoparticles $a = 104$ and $b = 52$ nm (3). Data presented for 0−600 AB cycles of TMA and water. (B) Out-of-plane height dependence of the short-range distance dependence for the Ag triangular nanoparticles $a = 90$ and $b =$ (1) 30, (2) 40, and (4) 51 nm, and Ag hemispherical nanoparticles $a = 104$ and $b = 52$ nm (3). Data presented for 0−20 AB cycles of TMA and water. Linear regression was used to fit the data to lines described by the following equations: $y = 1.7x + 9.1$, $R^2 = 0.9602$ (1); $1.0x + 3.5$, $R^2 = 0.9689$ (2); $1.2x + 7.0$; $R^2 = 0.9293$ (3); $y = 0.5x + 0.1$, $R^2 = 0.9744$ (4).

that the LSPR sensors possess angstrom-level sensitivity to the Al_2O_3 thickness changes.

Previous results have shown that hemispheroidal nanoparticles have a smaller sensing distance than triangular nanoparticles of similar volume.[7] Unexpectedly, Figure 7B-3 shows that the hemispheroidal particles ($a = 104$ and $b = 52$ nm) presented here have a larger LSPR λ_{max} shift at long distances compared with triangular nanoparticles with $a = 90$ and $b = 51$ nm (Figure 7A-4). Also, at short distances from the nanoparticle surface, the hemispheroidal particles have larger LSPR λ_{max} shifts than

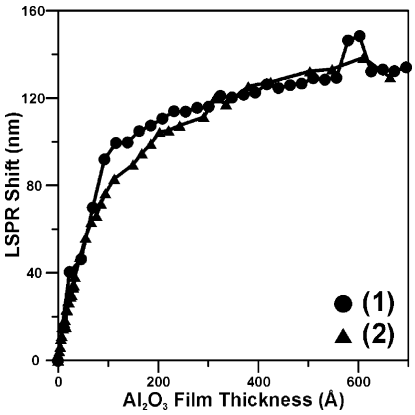

Figure 8. Comparison of the calculated (1) and experimental (2) shifts of the LSPR from bare truncated tetrahedral particles with $a = 90$ and $b = 40$ nm.

both triangular nanoparticles with $a = 90$ and $b = 40$ and 51 nm.

Theory. Using the discrete dipole approximation (DDA) method,[21−24] we modeled the LSPR λ_{max} shift measurements for silver particles coated with multilayers of Al_2O_3. In this method, the particle and Al_2O_3 coating are represented using a cubic grid of polarizable elements, with the polarizability of each element determined by the local dielectric constant. The particles are represented either as a truncated tetrahedron or as a hemispheroid, with dimensions taken to match the experimental results. The grid size in these calculations is 2 nm, and the wave vector is taken perpendicular to the bottom surfaces of the truncated tetrahedron or hemispheroid. The refractive index of silver is taken from Hunter and Lynch[25] and that for the adsorbate Al_2O_3 is taken to be 1.57 from the experimental data. The resonance wavelength of the truncated, tetrahedron-shaped silver particles was calculated with the layer thickness of the Al_2O_3 taken to be the grid size, 2 nm. This is not the same as the layer thickness of Al_2O_3; however, the dependence of the LSPR λ_{max} shifts on the layer thickness is not sensitive to this difference for layers that are more than around 5 nm thick (as is apparent from Figure 8). Figure 8 shows excellent agreement between the experimental and calculated results for the truncated tetrahedral shape. These results are similar to what we obtained in previous work involving the long-range dependence of the LSPR λ_{max} shifts using 11-MUD/ Cu^{2+} multilayers, but here the index of refraction of the Al_2O_3 is known accurately, whereas, with the SAM multilayers, it could only be estimated.[7] The only significant differences between theory and experiment in Figure 8 are (1) that the theory shift is higher than that of experiment for layer thicknesses of 10−30 nm and (2) a small bump in the calculated result at 50 nm. The 10−30 nm result

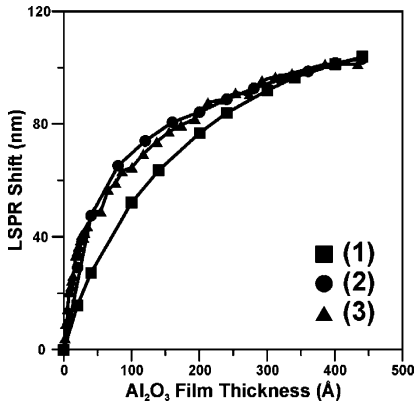

Figure 9. Experimental (▲) vs calculated shift (■) of the LSPR from bare hemispheroidal particles with $a = 104$ and $b = 52$ nm. A second calculation (●) was conducted with a small ring added to the hemispheroid as described above.

could easily arise from small differences between theory and experiment in the precise definition of the layer structure. The bump is likely a photonic resonance effect that would be extremely sensitive to layer structure and thus is unlikely to show up in the same way in the experiment.

The hemispheroidal nanoparticle was modeled using the same parameters as the triangular nanoparticle. Initially, the hemispheroidal nanoparticle was modeled as half an ellipsoid with dimensions of diameter = 104 nm and height = 52 nm. The nanoparticle was then coated with layers of Al_2O_3. The calculated results as well as the LSPR λ_{max} shifts from the experiment are presented in Figure 9. This shows, as noted earlier, that the measured LSPR λ_{max} red shifts sharply with increasing Al_2O_3 film thickness for layer thicknesses less than 10 nm and then bends over as the thickness is increased. However, the calculations show that the LSPR λ_{max} red shifts more slowly with increasing Al_2O_3 layer thickness for thickness below 10 nm, with a slope that is significantly smaller than is observed. Thus, it seems that even though the particle was modeled using the exact shape parameters from the experiment, the model does not describe the observed sensitivity to layer thickness. Further, the difference between theory and experiment is consistent with the presence of a short-range near field around the hemispheroidal particle, such as would arise from small radius of curvature features such as the sharp points that are present in the truncated tetrahedral structure. From this we infer that the idealized hemispheroidal shape does not characterize the annealed particle completely and there must be additional sharp features, not resolvable with AFM, that produce the short-range near-field behavior that is seen in the experiments. To model this, we have assumed that at the bottom edge of each spheroid, there is an "apron" of metal that arises from wetting the substrate during the annealing stage. Thus, the hemispheroidal nanoparticle is assumed surrounded by a ring of metal that is 8 nm in width and 4 nm in height whose bottom surface is parallel to the bottom surface of the hemispheroid. The results of DDA calculations with this structure (Figure 9) agree well with the experimental LSPR λ_{max} shifts. From this we see how a small, sharp feature on the nanoparticle can have a large influence on the nearfield and hence on the short-range dependence on layer thickness. This influence becomes less important when the layer thickness is increased, especially when the layer thickness is larger than 30 nm. Unfortunately, we do not have the resolution in our AFM measurements to see a feature as small as is suggested by the theory. Also, instead of an apron, a crack of similar dimensions but underneath the bottom of the particle should have a similar affect.

Conclusions

This work demonstrates that the LSPR nanosensor can detect a single layer of Al_2O_3 deposited by ALD. Furthermore, the long-range results presented in this paper provide a 10x increase in the spatial resolution compared with previous experiments. At short distances from the Ag nanoparticle surface, there is a much larger LSPR λ_{max} red shift than is seen at distances further from the nanoparticle surface. Furthermore, nanoparticles with fixed in-plane widths and decreasing out-of-plane heights have larger sensing distances, which is the same trend that was observed for alkanethiol layers at larger distances from the nanoparticle surface. Surprisingly, it was found that hemispheroidal nanoparticles show sensitivity to adsorbed layers that is comparable to that for the triangular nanoparticles. This work has also explored the nucleation and growth mechanism of Al_2O_3 by ALD on Ag surfaces. Both XPS and QCM results suggest that initially, TMA decomposes completely on the Ag surface.

Acknowledgment. This work was supported by the Chemical Sciences, Geosciences and Biosciences Division, Office of Basic Energy Sciences, Office of Science, U.S. Department of Energy (DE-FG02-03ER15457) the Northwestern University Institute for Environmental Catalysis, the NSF Network for Computational Nanotechnology, the NSF (EEC-0118025, DMR-0076097, CHE-0414554), and the Air Force Office of Scientific Research MJURI program (F49620-021-0381). ALD was conducted at Argonne National Laboratory and was supported by the U.S. Department of Energy, BES-Materials Sciences (W-31-109-Eng-38). We are also grateful to the Electron Microscopy Center at Argonne National Laboratory, which is supported by the DOE Office of Science (W-31-109-Eng-38).

References and Notes

(1) Haes, A. J.; Haynes, C. L.; McFarland, A. D.; Schatz, G. C.; Van Duyne, R. P.; Zou, S. *MRS Bull.* **2005**, *30*, 368−375.

(2) Haes, A., J.; Van Duyne, R. P. *J. Am. Chem. Soc.* **2002**, *124*, 10596−10604.

(3) Riboh, J. C.; Haes, A. J.; McFarland, A. D.; Yonzon, C. R.; Van Duyne, R. P. *J. Phys. Chem. B* **2003**, *107*, 1772−1780.

(4) Haes, A. J.; Chang, L.; Klein, W. L.; Van Duyne, R. P. *J. Am. Chem. Soc.* **2005**, *127*, 2264−2271.

(5) Yonzon, C. R.; Jeoung, E.; Zou, S.; Schatz, G. C.; Mrksich, M.; Van Duyne, R. P. *J. Am. Chem. Soc.* **2004**, *126*, 12669−12676.

(6) Jung, L. S.; Campbell, C. T.; Chinowsky, T. M.; Mar, M. N.; Yee, S. S. *Langmuir* **1998**, *14*, 5636−5648.

(7) Haes, A. J.; Zou, S.; Schatz, G. C.; Van Duyne, R. P. *J. Phys. Chem. B* **2004**, *108*, 109−116.

(8) Malinsky, M. D.; Kelly, K. L.; Schatz, G. C.; Van Duyne, R. P. *J. Am. Chem. Soc.* **2001**, *123*, 1471−1482.

(9) Haes, A. J.; Zou, S.; Schatz, G. C.; Van Duyne, R. P. *J. Phys. Chem. B* **2004**, *108*, 6961−6968.

(10) Ritala, M.; Leskela, M. *Handb. Thin Film Mater.* **2002**, *1*, 103−159.

(11) Ott, A. W.; Klaus, J. W.; Johnson, J. M.; George, S. M. *Thin Solid Films* **1997**, *292*, 135−144.

(12) Groner, M. D.; Fabreguette, F. H.; Elam, J. W.; George, S. M. *Chem. Mater* **2004**, *16*, 639−645.

(13) Jensen, T. R.; Duval, M. L.; Kelly, K. L.; Lazarides, A. A.; Schatz, G. C.; Van Duyne, R. P. *J. Phys. Chem. B* **1999**, *103*, 9846−9853.

(14) Elam, J. W.; Groner, M. D.; George, S. M. *Rev. Sci. Instrum.* **2002**, *73*, 2981−2987.

(15) Rocklein, M. N.; George, S. M. *Anal. Chem.* **2003**, *75*, 4975−4982.

(16) Matero, R.; Rahtu, A.; Ritala, M.; Leskela, M.; Sajavaara, T. *Thin Solid Films* **2000**, *368*, 1−7.
(17) Moulder, J. F.; Stickle, W. F.; Sobol, P. E.; Boman, K. D. *Handb X-Ray Photoelectron Spectrosc.* **1992**.
(18) Groner, M. D.; Elam, J. W.; Fabreguette, F. H.; George, S. M. *Thin Solid Films* **2002**, *413*, 186−197.
(19) Zhou, X. L.; White, J. M. *Surf. Sci.* **1992**, *273*, 322−340.
(20) Rahtu, A.; Alaranta, T.; Ritala, M. *Langmuir* **2001**, *17*, 6506−6509.
(21) Draine, B. T.; Flatau, P. J. *J. Opt. Soc. Am. A* **1994**, *11*, 1491.
(22) Draine, B. T.; Flatau, P. J. *User Guide for the Discrete Dipole Approximation Code DDSCAT. 6.0*, 2003, http://arxiv.org/abs/astro-ph/0309069.
(23) Kelly, K. L.; Coronado, E.; Zhao, L. L.; Schatz, G. C. *J. Phys. Chem. B* **2003**, *107*, 668−677.
(24) Zou, S.; Zhao, L.; Schatz, G. C. *Proc. SPIE-Int. Soc. Opt. Eng.* **2003**, *5221*, 174−181.
(25) Lynch, D. W.; Hunter, W. R.; Palik, E. D. *Handbook of Optical Constants of Solids*; Academic Press: New York, 1985.